Nano Research

Open Access

Research Article

# $Li_2CO_3$-rich interphase construction via alternating pulse current-driven $CO_2$ reduction for high performance $LiFePO_4$/graphite full-cell

Yueqin Kong[1,2], Shiyou Li[1,2,3], Peng Wang[1,2,3], Yin Quan[1,2], Huanhuan Yang[1,2], Dingdong Hao[1,2], Lijuan Wang[1,2], Juan Bai[1,2], Tiaotiao Lu[1,2], Dongni Zhao[1,2,3], and Xiaoling Cui[1,2,3] ✉

[1] *School of Petrochemical Technology, Lanzhou University of Technology, Lanzhou 730050, China*
[2] *Key Laboratory of Low Carbon Energy and Chemical Engineering of Gansu Province, Lanzhou 730050, China*
[3] *Gansu Province Engineering Research Center for Waste Resource Utilization and Waste Materials in New Energy Industry, Lanzhou 730050, China*

**Cite this article:** *Nano Research*, **2026**, *19*, 94908818. https://doi.org/10.26599/NR.2026.94908818

**ABSTRACT:** Featuring of low $Li^+$ diffusion barrier and high $Li^+$ conductivity, a $Li_2CO_3$-rich solid electrolyte interphase (SEI) is critical for improving the energy density and cycle life of lithium-ion batteries. As a gaseous additive, $CO_2$ can be added into the electrolyte to *in situ* generating $Li_2CO_3$-contained SEI. However, $CO_2$-derived SEI formation is kinetics limitation. Here, we identify the adsorption of CO intermediate products impeding the full conversion of $CO_2$, and furtherly apply an alternating pulse current (APC) discharge to desorb CO and promote the $CO_2$ decomposition, ultimately *in-situ* forming a uniform, smooth, and $Li_2CO_3$-rich SEI in the first cycle. Owing to the excellent $Li^+$ transport capability and structural stability, this APC-formed SEI enables lithium/graphite (Li/Gr) half-cells achieving a high rate performance (5 C, 180 mAh·g$^{-1}$, and 80.1% after 170 cycles), exceeding currently advanced cells with $Li_2CO_3$-contained SEI. Furthermore, we directly employ the Gr anode with the APC pre-formed $Li_2CO_3$-rich SEI to assemble $LiFePO_4$ (LFP)/Gr full-cell. Advantaged by the high $Li^+$ diffusivity and stability, this pre-formed SEI not only compensates for the active lithium loss, dramatically enhancing the initial coulombic efficiency from 69.2% to 91.7%, but also substantially increases the discharge capacity and long-term cycling stability (131.8 mAh·g$^{-1}$ after 100 cycles at 0.5 C). This straightforward strategy simultaneously enhances gas additive utilization efficiency and constructs a robust electrolyte/electrode interphase, demonstrating a dual-optimization approach through electrolyte design and interface engineering for high-performance batteries.

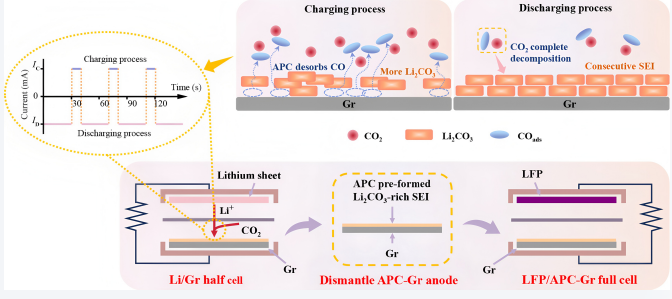


**KEYWORDS:** lithium-ion batteries (LIBs), $Li_2CO_3$, solid electrolyte interphase, $CO_2$ additive, pulse current

## 1 Introduction

The escalating global demand for renewable energy has driven the development of large-scale energy storage technologies to ensure reliable power supply. Electrochemical energy storage has emerged as a critical enabler for stable electricity provision and the efficient utilization of clean energy [1–3]. Among these technologies, lithium-ion batteries (LIBs) dominate applications from electric vehicles and portable electronics to grid-scale storage, owing to their high energy density and superior cycling performance [4, 5]. However, the practical performance and safety of these batteries are fundamentally governed by the solid electrolyte interphase (SEI), a passivation layer formed through irreversible electrochemical decomposition of the electrolyte at the anode surface [6, 7]. A well-constructed SEI kinetically suppresses further electrolyte reduction because of the electron insulation, and facilitates ion transport across the electrode/electrolyte interface, thereby significantly enhancing the long-term cycling stability of batteries.

In-depth explorations have proved that the SEI formed by commercial electrolyte decomposition is generally composed of an inorganic inner and an organic outer [8]. Increasing the content of the inorganic layer (mainly lithium fluoride (LiF), lithium

**Received:** March 21, 2026; **Revised:** April 29, 2026
**Accepted:** May 7, 2026

✉Address correspondence to xlcuilw@163.com

carbonate ($Li_2CO_3$)) benefits to improving the ionic conductivity and electronic insulation, thermodynamically and mechanical stability of the SEI [9]. For graphite anodes, $Li_2CO_3$ exhibits superior physicochemical compatibility compared to LiF. Although LiF is valued for its wide bandgap and chemical inertness [10], its high $Li^+$ diffusion barrier (0.729 eV) can impede interfacial transport relative to graphite (0.308–0.400 eV) [11]. In contrast, $Li_2CO_3$ presents a lower and well-matched $Li^+$ migration barrier (0.227–0.491 eV) and tends to form a continuous, dense and smooth structure that conforms closely to the graphite surface, effectively suppressing electrolyte parasitic reactions and graphite exfoliation [12, 13]. Moreover, $Li_2CO_3$ possesses a good mechanical strength, which is the key to bear the volume change of graphite anode during the repeated charging and discharging cycles [14]. Therefore, constructing a $Li_2CO_3$-rich SEI may be desired for commercial LIBs to enhance the cycling performance and rate capability. In addition, due to the higher $Li^+$-conductivity and chemical-mechanical stability, applying the graphite anode with pre-generated $Li_2CO_3$-rich SEI to the full-cell is expected to compensate for the active lithium loss caused by the formation of SEI during the first cycle, thereby improving the initial columbic efficiency, reversible capacity and cycling performance of the full-cell, indirectly achieving pre-lithiation lithium replenishment of full-cell.

Several methods have been reported for constructing a $Li_2CO_3$-rich SEI, such as dispersing $Li_2CO_3$ powder within electrode materials [15], coating carbon materials with an aqueous $Li_2CO_3$ solution [16], and directly growing $Li_2CO_3$ thin films via atomic layer deposition [17]. However, these approaches are complex, costly, and difficult to align with the scalability and economic requirements of commercial LIBs manufacturing. Recently, directly introducing $CO_2$ as a gaseous additive into the electrolyte has been proposed as an effective strategy to form a $Li_2CO_3$-rich SEI [18–20]. Our group have found that adding $CO_2$ additive not only enabled the *in-situ* formation of $Li_2CO_3$-rich SEI on the graphite anode, but also altered the solvation structure of $Li^+$, thereby reducing the desolvation energy barrier of $Li^+$ and improving the ion-transport kinetics at the electrode/electrolyte interface. However, current researches merely highlight the benefits of $CO_2$-derived $Li_2CO_3$-rich SEI, with scant investigation into the film-formation kinetics of gaseous additives. Crucially, whether the added $CO_2$ fully decomposes and results in a sufficiently effective SEI has not been involved, leaving the relationship between additive amount and performance efficacy unclear.

We previously certified that the decomposition of film-formation additives such as lithium difluorooxalate borate (LiDFOB), lithium bis(oxalate)borate (LiBOB), and lithium difluoro bis(oxalate) phosphate (LiDFBOP), was incomplete and formed a organics-dominated SEI during the first traditional constant current discharging (CC) process [21, 22]. Therefore, we developed the strategy of applying external physical field (ultrasound, negative electrical field) to promote the additives decomposition and strengthen the formation of inorganics-rich SEI, achieving the goal of "amount reduction and efficiency increase" [22]. Moreover, the pulse technology has recently been explored in the battery formation processes to improve the SEI formation kinetics [23], where the periodically switching electric field significantly regulated the interfacial reaction, enhanced the ion conductivity and mechanical stability of the resulting SEI.

In light of these investigations, the $CO_2$-derived SEI construction process was firstly deeply enquired. We found that the CC discharge led to the formation of inconsecutive $CO_2$-derived SEI, which originated from that the generated CO intermediate adsorbed on the graphite surface, impeding the continuous decomposition of $CO_2$. Hence, alternating pulse current (APC) discharge was applied to promote $CO_2$ decomposition and *in-situ* form a uniform, dense and smooth, and $Li_2CO_3$-rich SEI. Owing to the high $Li^+$ diffusive and structural stability of such SEI, the lithium/graphite (Li/Gr) half-cell achieved a capacity retention of 80.1% after 170 cycles at 5 C. Moreover, introducing this Gr anode with pre-formed $Li_2CO_3$-rich SEI into $LiFePO_4$ (LFP)/Gr full-cell, not only this pre-formed SEI compensated for the active lithium loss, dramatically enhancing the initial coulombic efficiency of full-cell from 69.2% to 91.7%, but also the electrochemical-mechanical stable and $Li^+$ conductive $Li_2CO_3$-rich SEI substantially increased discharge capacity and exceptional long-term cycling stability (131.8 $mAh{\cdot}g^{-1}$ after 100 cycles at 0.5 C). This simple formation strategy fundamentally improves the utilization efficiency of gaseous additives and constructs an excellent $Li_2CO_3$-rich SEI, broadening the application route towards high-performance battery through both electrolyte formulation design and interface engineering.

## 2 Experimental

### 2.1 Material preparation

1.0 M $LiPF_6$ in ethylene carbonate/diethyl carbonate (EC/DEC 1:1, v/v) electrolyte was purchased from Chaoyang Yongheng Chemical Co., Ltd. $CO_2$ gaseous additive was introduced into the above electrolyte in the form of dry ice (solid $CO_2$, 99.9%) and brought to saturation to generate the electrolyte with saturated $CO_2$. The graphite (Gr) and $LiFePO_4$ (LFP) slurries were formulated by blending 10 wt.% polyvinylidene fluoride (PVDF, 99.6%), 80 wt.% Gr (99.9%) or LFP (99.9%), and 10 wt.% acetylene black in N-methyl-2-pyrrolidone (NMP, 99.9%). And then the Gr and LFP slurries were coated on the copper foil and aluminum foil, respectively. Followed by drying, the Gr anode and LFP cathode with a diameter of 14 mm were obtained. The CR2025 type Li/Gr half-cells and LFP/Gr full-cells were assembled with Gr anode, Celgard 2400 separator and 40 μL of electrolyte, using lithium foil and the as-fabricated LFP cathode as the counter electrodes in the half-cell and full-cell configurations, respectively. All the assembly were performed in an argon (Ar)-filled glove box with water and oxygen content below 0.1 ppm.

### 2.2 Electrochemical evaluation

The Li/Gr half-cell was cycled within a voltage range of 2.0–0.01 V at 0.5 or 5 C. For the LFP/Gr full-cell, the anode-to-cathode capacity ratio (N/P ratio) was set to 1.05:1, and cycling tests were performed from 2.5 to 4.2 V at 0.5 C. A repeated discharge-standing test was employed to study the $CO_2$ reduction reaction. Specifically, the Li/Gr half-cell was first discharged from the open-circuit voltage (OCV) to 0.60 V, followed by a 40 h standing period to mitigate concentration polarization and then discharged again to 0.60 V to assess whether the reaction had reached completion. Additionally, galvanostatic intermittent titration technique (GITT) measurements were conducted by charging/discharging the Li/Gr half-cell at 0.1 C for 10 min, each followed by a 30 min relaxation interval. All the above-mentioned electrochemical experiments were carried out on an DH7006 electrochemical workstation (Donghua, Jiangsu, China). Electrochemical impedance spectroscopy (EIS) was carried out on a Donghua 7000C electrochemical workstation (Jiangsu, China) with a 5 mV AC amplitude over a frequency range of $10^5$–$10^{-2}$ Hz. Potential-resolved

*in situ* electrochemical impedance spectroscopy (PRIs-EIS) of Li/Gr half-cells was conducted on a Chi920d workstation (Chenhua, Shanghai, China). A series of EIS measurements were taken from 2.0 to 0.01 V to characterize the real-time interfacial properties at different staircase equilibrium voltages, with a 5 mV step between adjacent tests. And the sinusoidal AC perturbation amplitude of each individual EIS test was 5 mV, and the frequency range was $10^5$–$10^{-1}$ Hz. Scanning electrochemical microscope (SECM) tests were also conducted on CHI920D using a four-electrode system, where CHI116 microprobe (Chenhua, Shanghai, China, with the diameter of 10 um) and graphite electrode is the first and second working electrodes, lithium foil is the reference electrode and platinum wire is the counter electrode. Differential electrochemical mass spectrometry (DEMS, Shanghai Linglu Instrument QMG100) was employed as an *in-situ* technique to investigate CO desorption and the enhanced $CO_2$ conversion under APC mode.

### 2.3 Physicochemical characterization

The SEI component composition was examined using X-ray photoelectron spectroscopy (XPS, Kratos AXIS ULTRADLD, UK). The structures of the SEI were analyzed using atomic force microscope (AFM, NX10, Park), scanning electron microscope (SEM, ZEISS Sigma 300), and transmission electron microscopy (TEM, JEOL JEM -F200). Before these analyses, the cells all underwent five cycles to ensure the complete formation of the SEI. The relative contents of Li in the graphite anode were measured by inductively coupled plasma optical emission spectrometer (ICP-OES, iCAP PRO XP Duo).

### 2.4 Theoretical calculation

Density functional theory (DFT) calculations were performed using the Vienna *ab initio* simulation package (VASP) with the Perdew–Burke–Ernzerhof (PBE) exchange-correlation functional within the generalized gradient approximation. The projector augmented wave (PAW) method was employed, and van der Waals interactions were accounted for using the DFT-D3 correction. The graphite edge was modeled by a two-layer 4 × 4 graphene sheet with armchair termination, and a vacuum layer of at least 10 Å was introduced to avoid periodic interactions. A plane-wave cutoff energy of 500 eV was used, and the Brillouin zone was sampled with a gamma-centered k-point mesh. Geometry optimizations were converged until the forces on all atoms were below 0.02 eV·Å$^{-1}$ and the energy change was less than $10^{-5}$ eV. Adsorption energies ($E_{ads}$) for $CO_2$ and CO were calculated as

$$E_{ads} = E_{total} - E_{molecule} - E_{graphite}$$

where $E_{total}$ is the total energy of the adsorbed system, $E_{molecule}$ is the energy of the isolated molecule in vacuum, and $E_{graphite}$ is the energy of the pristine graphite edge.

## 3 Results and discussion

### 3.1 APC discharge promotes $CO_2$ complete reduction

Apart from the decomposition of $LiPF_6$ at 1.3 V, the initial discharge differential capacity (d$Q$/d$V$) curves (Fig. S1 in the Electronic Supplementary Material (ESM)) for Li/Gr cells in $LiPF_6$-EC/DEC electrolyte with $CO_2$ under CC discharge distinguish two reduction peaks in the range of 0.5–0.8 V, where the peak near 0.74 V attributes to the EC decomposition, and the peak at approximately 0.78 V corresponds to the $CO_2$ reduction to form $Li_2CO_3$ [24, 25]. By elucidating the reduction process of $CO_2$ with repeated discharge-standing experiments (Fig. 1(a)), we observe an anomalous phenomenon that compared to the counterpart of standing 0 h, after experiencing 1st discharge and standing for 40 h, Li/Gr cell with $CO_2$ still display the $CO_2$ reduction peak at about 0.78 V in the 2nd discharge, preliminarily indicating that $CO_2$ is not completely decomposed during the 1st discharge. And the leftward shift of $CO_2$ reduction peak also confirms that the solid products generated from $CO_2$ reduction deposit on the graphite surface, forming the SEI containing $Li_2CO_3$ but leading to electrode polarization [26, 27]. This suggests that intermediates formed during the reduction reaction may hinder further reduction of $CO_2$, but after standing for enough time, these intermediates presumably diminish or disappear, allowing the $CO_2$ reduction to proceed. To track the real-time evolution of the interface during the first discharge of Li/Gr half-cells, we performed potential-resolved *in situ* electrochemical impedance spectroscopy (PRIs-EIS) tests and used distribution of relaxation times (DRT) analysis [28, 29]. A standing time of 0 and 5 s were selected as the minimum and reference time intervals, respectively, to investigate the influence of different standing time on the interfacial properties. As shown in Figs. 1(b) and 1(c), there appears clear difference for the characteristic peak in the $10^{-2}$ s, which represents the $R_{SEI}$. Specifically, after standing for 5 s, the $R_{SEI}$ intensity decreases from 0.78 V ($CO_2$ reduction to form $Li_2CO_3$), while that of standing for 0 s remains a relatively high $R_{SEI}$. This indicates that the SEI formation from $CO_2$ decomposition into $Li_2CO_3$ is diffusion-limited. That is, given enough diffusion time, $CO_2$ would continuously decompose to form a $Li_2CO_3$-contained SEI, thereby decreasing the $R_{SEI}$ for the high $Li^+$-conductivity. Otherwise, the generated intermediates would accumulate on the graphite surface, hindering the formation of $Li_2CO_3$ rather than decreasing the interface impedance. The DRT-PRIs-EIS results get the same inference with repeated discharge-standing experiments. Subsequently, we deduced the electrochemical reduction of $CO_2$ yielding $Li_2CO_3$, in which Eq. (1) represents the overall reaction [30, 31] and Eqs. (2) and (3) are the likely elementary steps [30, 32]

$$Li^+ + 3CO_2 + 4e^- \rightarrow 2Li_2CO_3 + C \quad (1)$$

$$2CO_2 + 2e^- \rightarrow CO_3^{2-} + CO_{ads} \quad (2)$$

$$CO_2 + CO_{ads} + 4e^- \rightarrow CO_3^{2-} + C \quad (3)$$

Combining the theory calculation, the film-formation mechanism of a $CO_2$-derived $Li_2CO_3$-rich SEI in the CC discharge is described as follows. First, $CO_2$ gains electrons to undergo reduction to form $Li_2CO_3$ and the intermediate CO (Eq. (2)). Next, the CO further reacts with $CO_2$ and $Li^+$ to produce more $Li_2CO_3$ (Eq. (3)). However, the CO formed in Eq. (2) exhibits a stronger adsorption affinity toward the graphite anode surface than $CO_2$ (Fig. 1(d)), which leads to its preferential adsorption and significant accumulation [33]. Concurrently, the $Li_2CO_3$ formed in Eq. (2) hinders the direct contact between $CO_2$ and the adsorbed CO, thereby reducing the number of active sites available for $CO_2$ conversion. This greatly reduces the utilization efficiency of the $CO_2$ gaseous additive, resulting in the formation of inconsecutive SEI displayed in Fig. S2 in the ESM. And Fig. 1(e) illustrates the mechanism of the limitation for $CO_2$ decomposition in the CC

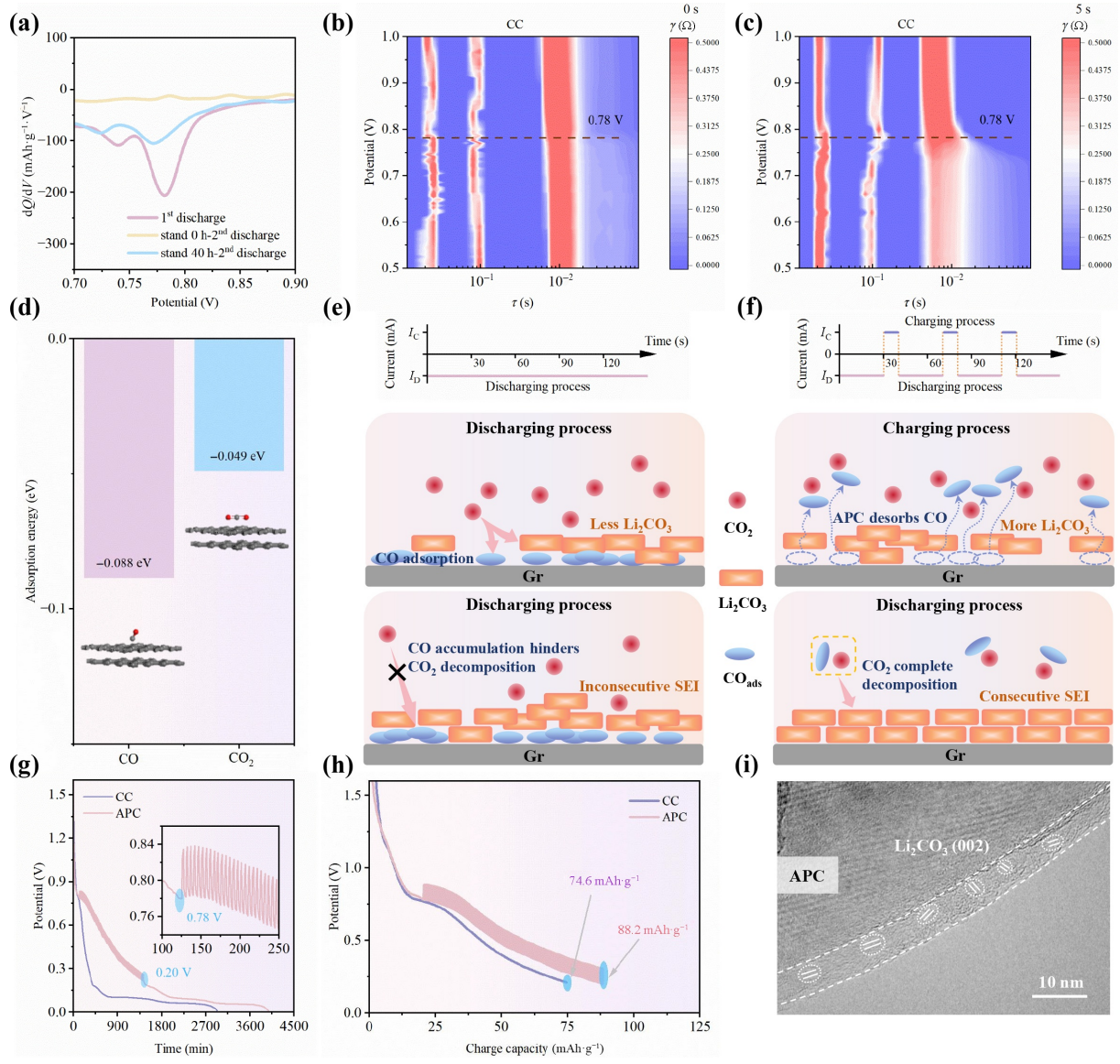


**Figure 1** (a) Differential capacity curves under repetitive discharge-standing test with the cut-off voltage of 0.60 V (vs. Li/Li$^+$), and the standing time is 0 and 40 h, respectively. Contour map of DRT analysis for the PRIs-EIS tests in the initial discharge, where the standing time for each step potential is (b) 0 and (c) 5 s. (d) Adsorption energies of $CO_2$ and CO on the graphite anode surface. Schematic diagram of $CO_2$-derived $Li_2CO_3$-rich SEI formed under (e) CC and (f) APC discharge protocol. Characterization of the $CO_2$ reduction reaction during the first discharge under APC and CC modes: (g) potential-time curve, (h) potential-capacity curve. (i) TEM image of the formed SEI during the first APC discharge.

discharge.

Therefore, to facilitating the diffusion of the CO intermediate and preventing its local over-accumulation, we applied APC discharge technique [34], which consists of a constant-current charge for 10 s ($I_C$ = 0.03 mA, $t_C$ = 10 s) immediately followed by a constant-current discharge for 30 s (($I_D$ = 0.03 mA, $t_D$ = 30 s)) in the range from 0.78 V ($CO_2$ reaction potential) to 0.2 V (SEI-formation cutoff potential) to enhance the reaction of $CO_2$ towards the formation of $Li_2CO_3$-rich SEI. Specifically, the charging and discharge current of 0.03 mA are selected because a lower formation current favors of minimizing polarization and forming a more uniform and stable SEI [35]. And using the redox competition mode of SECM determines the charging time of 10 s [22, 23]. We firstly perform probe approach test to fix the probe position (Fig. S3(a) in the ESM), and then replace the redox media as $CO_2$-added electrolyte and applied the potential of 0.78 V which corresponds to the reduction potential of $CO_2$ to CO on both the graphite substrate and probe electrode. Figure S3(b) in the ESM shows a clear drop inflection point of the probe current at 10 s, indicating that the time CO diffuses from the substrate to the probe is 10 s. Thereby, setting the charging plus time as 10 s can effectively desorb CO and enables the sufficient reaction of $CO_2$ to form $Li_2CO_3$. In addition, the discharging time of 30 s is obtained by comparing the inorganics content in the SEI formed under different discharging time using AFM phase images (Fig. S4 in the ESM). The SEI formed with a 30 s discharge exhibits the most negative phase angle, signifying the highest content of inorganic $Li_2CO_3$ [34, 36], which is in favor of improving mechanical stability and $Li^+$ conductivity. Consequently, the persistent optimized AC protocols (30 s discharge with 0.03 mA and then 10 s charge at 0.03 mA) are adopted in the first discharge of 0.78–0.2 V.

Schematic illustrations of the APC discharge to form $CO_2$-

derived $Li_2CO_3$-rich SEI is presented in Fig. 1(f). Unlike the CC discharge, the introduced APC charge process facilitates the diffusion of accumulated intermediate CO from the interface into the bulk electrolyte. This not only promotes the subsequent consumption of the CO intermediate to generate more $Li_2CO_3$, but also allows the CO that diffuses into the electrolyte to maintain contact with $CO_2$ in subsequent discharge steps, thereby continuing to react on the graphite surface to produce more $Li_2CO_3$. Thus, this strategy promotes the complete reduction of the $CO_2$, alleviates charge accumulation on the graphite surface and reduces cell polarization, as well as extends the duration of $CO_2$ participation in the reaction, leading to the potential plateau near 0.78 V significantly prolonged (Fig. 1(g)). Accordingly, the discharge capacity provided by $CO_2$ decomposition increases from 74.6 to 88.2 mAh·g$^{-1}$ (Fig. 1(h)), and the corresponding initial discharge capacity increases as well (Fig. S5 in the ESM). And the transmission electron microscope (TEM) in Fig. 1(i) demonstrates a uniform and consecutive SEI covered on graphite surface, strongly confirming that the APC mode not only enhances the $CO_2$ decomposition, but also benefits to the homogenous deposition of $Li_2CO_3$.

To directly verify the CO desorption and enhanced $CO_2$ conversion in the APC mode, we conducted *in-situ* DEMS measurements during the first discharge of Li/Gr half-cells under both CC and APC modes (Fig. S6 in the ESM). In the APC mode, when discharging to 0.78 V, the $CO_2$ signal decreased while the CO signal emerged and increased, directly evidencing the reduction of $CO_2$ to CO. The subsequent detection of CO in the gas phase indicates that the adsorbed CO is desorbed from the graphite surface, enabled by the pulsed reverse charging in the APC. In contrast, under the CC mode, no detectable CO signal throughout the discharge confirms again the strong adsorption affinity of CO on graphite (Fig. 1(d)). Moreover, the consistently higher residual $CO_2$ signal substantiates that APC mode significantly enhance the $CO_2$ consumption.

### 3.2 APC constructs excellent $Li_2CO_3$-rich SEI

XPS analysis further validated the mechanism described above. Figure 2(a) compares the C 1s spectra of graphite electrode surfaces formed under CC and APC. Notably, the intensity of the C=O which belongs to $Li_2CO_3$ is markedly stronger under APC (Fig. 2(b)), indicating that APC discharge effectively promotes $CO_2$ reduction, thereby increasing the $Li_2CO_3$ content within the SEI [37]. Correspondingly, AFM phase images (Figs. 2(c) and 2(d)) reveal that the APC-formed SEI formed exhibits a more negative phase angle relative to the CC-formed SEI, consistent with a higher inorganic content resulted from increased $Li_2CO_3$. SEM images in Fig. S7 in the ESM further show that the APC-formed SEI is smoother, whereas the CC-formed appears rougher. Moreover, the AFM height image of APC-formed SEI displays a more uniform distribution with lower height variation of −260 to 200 nm, while the height of CC-formed SEI varies from −378 to 227 nm (Fig. S8 in the ESM). This agrees with the conclusion drawn from the literatures that more $Li_2CO_3$ endows the SEI smoother and uniform morphology, which signifies a more stable SEI to resist side reactions [12, 13]. Kelvin probe force microscopy (KPFM) measurements (Fig. S9 in the ESM and Fig. 2(e)) indicate that the APC-formed SEI possesses a higher average electron work function (5.06 eV) compared to the CC-formed SEI (4.63 eV), suggesting enhanced suppression of electron tunneling. Figure S10 in the ESM displays statistical heat maps of Young's modulus for CC-formed and APC-formed SEI, and Fig. 2(f) demonstrates the higher result of APC-formed SEI, indicating improved mechanical stability. This is attributed to the higher inorganic $Li_2CO_3$ content induced during the APC. And the collective characterizations of SEM, KPFM and Young's modulus provide the evidences that the $Li_2CO_3$-rich SEI helps to suppress parasitic reactions and ensures the long-cycle stability. Furtherly, we carried out a serious of electrochemical tests to investigate the $Li^+$ transmission in the $Li_2CO_3$-rich SEI. Galvanostatic intermittent titration technique (GITT) measures the $Li^+$ diffusion coefficient ($D_{Li^+}$) of the graphite electrode, and the results in Fig. 2(g) show that due to the APC-formed $Li_2CO_3$-rich SEI, $D_{Li^+}$ reaches $5.477 \times 10^{-10}$ cm$^2$·s$^{-1}$ during the discharge, higher than the value of $3.131 \times 10^{-10}$ cm$^2$·s$^{-1}$ obtained in the CC-formed. And the EIS of Li/Gr cells in Fig. 2(h) substantiates both the impedances of charge transfer ($R_{ct}$) and $Li^+$ transmits through the SEI ($R_{SEI}$) of APC-formed cell are smaller than that of CC-formed [38]. Moreover, temperature-dependent EIS spectra from 302 to 323 K (Fig. S11 in the ESM) were analyzed to calculate two active energies for $Li^+$ transport through the SEI ($E_a$ ($R_{ct}$), Fig. 2(i)) and $Li^+$ desolvation at SEI ($E_a$ ($R_{SEI}$), Fig. 2(i)) according to the Arrhenius law, showing that the SEI formed under APC exhibits smaller $E_a$ ($R_{SEI}$) and $E_a$ ($R_{ct}$) (49.22 and 35.42 KJ·mol$^{-1}$, respectively) than CC-formed (54.07 and 42.07 KJ·mol$^{-1}$, respectively). This confirms again that attributable to the SEI rich in $Li_2CO_3$, the SEI formed under APC has higher $Li^+$ transport and easier $Li^+$ desolvation, in accordance with the GITT results. In light of these advantages of more homogeneous morphology, higher inorganic and $Li_2CO_3$ content, and superior $Li^+$-conduction yet electron-insulation, this robust APC-formed SEI will have higher mechanical stability and improved $Li^+$ transport kinetics, portending better electrochemical performance of the battery.

### 3.3 APC-formed $Li_2CO_3$-rich SEI enhances the performance of Li/Gr cells

Benefiting from these structure and components merits, the Li/Gr cell with APC-formed SEI exhibits stable cycling performance, delivering a reversible capacity of 265.9 mAh·g$^{-1}$ with 78.7% capacity retention after 200 cycles at 0.5 C (Fig. 3(a)). In contrast, the cell with the CC-derived SEI shows marked capacity fading after only 100 cycles. Especially at higher rate, compared with that in CC (5 C, 110 mAh·g$^{-1}$, Fig. 3(b); 170 cycles, 41.9% capacity retention, Fig. 3(c)), the APC-formed cell has higher rate performance, with a higher charging specific capacity (5 C, 180 mAh·g$^{-1}$, Fig. 3(b)) and the slower capacity decay (170 cycles, 80.1% capacity retention, Fig. 3(c)), exceeding currently advanced cells with $Li_2CO_3$-contained SEI (Fig. 3(d)) [39–43].

The divergence in capacity fading can be attributed to the structural stability of the SEI, for which we made postmortem for the 100-cycled cells. For the CC-formed SEI, the SEM image in Fig. 3(e) appears some obvious cracks, and the TEM image in Fig. 3(f) exhibits rugged and rough structure, indicating severe side reactions between the graphite anode and the electrolyte, which results in non-uniform SEI growth in subsequent cycles. Accordingly, this structure deterioration leads to the higher interfacial impedance observed in the CC-formed SEI (Fig. 3(g)). In contrast, the APC-formed SEI remains intact and homogeneous, with almost no visible cracks (Figs. 3(h) and 3(i)). The robust structure of APC-formed SEI not only effectively suppresses continuous electrolyte decomposition but also facilitates the reversible $Li^+$ intercalation/deintercalation of the graphite electrode,

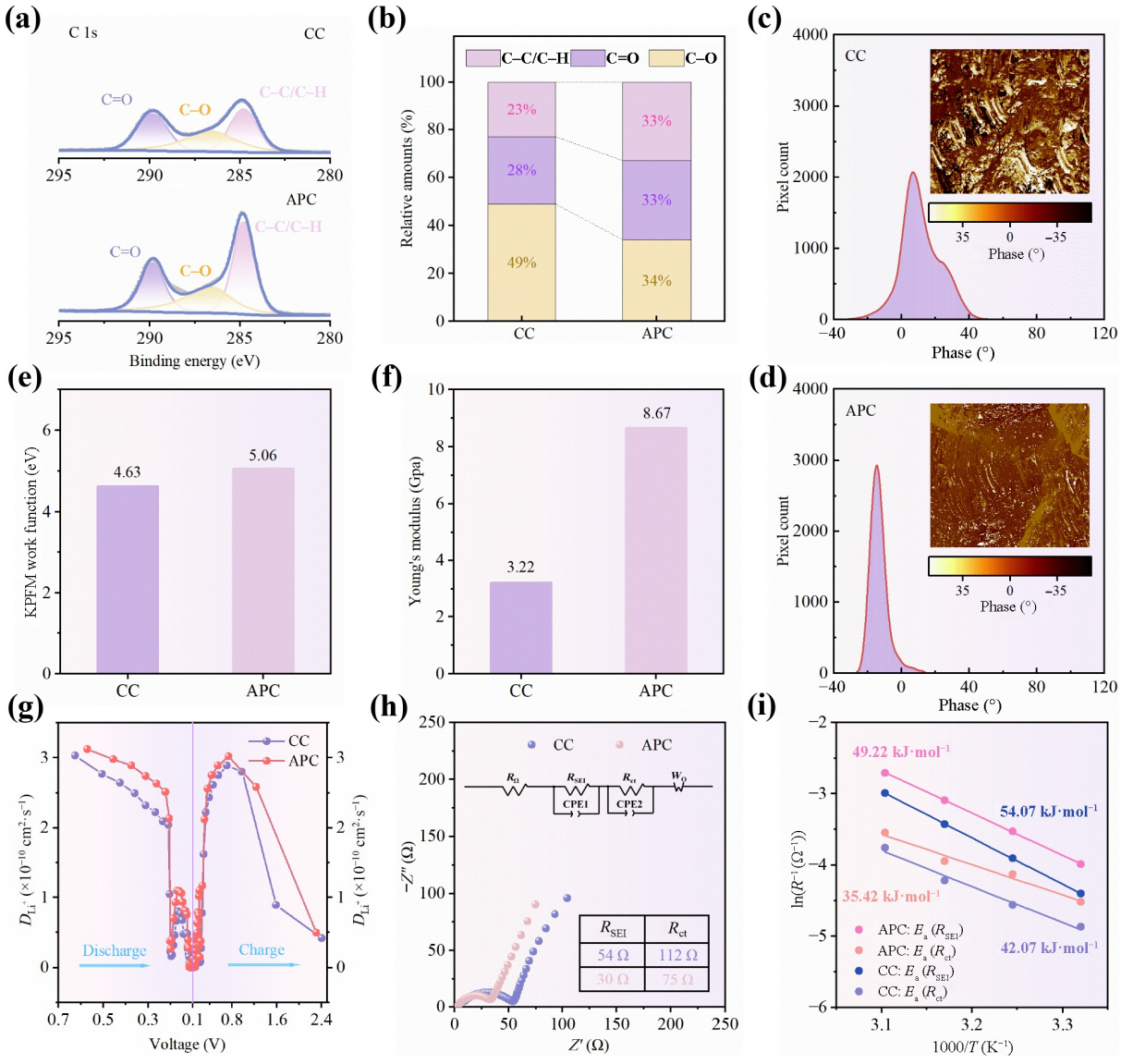


**Figure 2** XPS characterization of SEI components formed under APC and CC modes: (a) C 1s spectra and (b) comparison of C 1s XPS peak areas. (c) and (d) AFM phase angle diagram of the formed SEI under CC and APC. (e) KPFM histograms of the SEI formed under CC and APC. (f) Young's modulus histograms of the SEI formed under CC and APC. (g) $Li^+$ diffusion coefficients tested by GITT. (h) EIS Nyquist plots of the Li/Gr half-cells. (i) Arrhenius fitting of the $E_a$ ($R_{ct}$) and $E_a$ ($R_{SEI}$) curves for Li/Gr half-cells under CC and APC, derived from the temperature-dependent EIS spectra.

thereby enabling excellent electrochemical stability and rate capability during prolonged cycling.

### 3.4 APC pre-formed $Li_2CO_3$-rich SEI for full-cell pre-lithiation

Generally, the full-cell need to pre-lithiation to compensate the active lithium loss caused by the SEI formation in the first cycle (Fig. 4(a)) [44]. Here, to validate the advantages of the APC-formed $Li_2CO_3$-rich SEI, we furtherly assembled LFP/Gr full cells (LFP/APC-Gr), where the Gr anode is extracted from the Li/Gr half-cell which has experienced APC formation and formed a $Li_2CO_3$-rich SEI on the Gr surface (named APC-Gr). And LFP/Gr full-cells using pristine Gr as the anode were assembled as the controlled. All the full-cells use $CO_2$-added 1M $LiPF_6$-EC/DEC as electrolyte. Thus, utilizing a half-cell-preformed SEI for the subsequent full-cell assembly not only allows the evaluation of the APC-derived SEI but also represents a distinctive pre-lithiation strategy. Different from the conventional chemical pre-lithiation of the anode in a full cell [45–47], this strategy employs APC formation to promote the conversion of $CO_2$ and pre-form a $Li_2CO_3$-rich SEI on the Gr anode (Fig. 4(b)), thereby compensating for the substantial lithium consumption caused by $CO_2$ reduction in LFP/Gr full-cell. Therefore, this pre-lithiation method utilizes lithium from the Li metal in the half-cell to replenish lithium loss on the graphite anode, without consuming lithium ions from either the cathode or the electrolyte in the full cell. Inductively coupled plasma optical emission spectrometer (ICP-OES) was used to quantify lithium stored in the pre-formed SEI on the graphite anodes. Table S1 reveals that the APC-formed graphite anode contains 0.303 mmol Li per gram of graphite, providing direct evidence of the lithium reservoir in this pre-lithiation strategy. Thus initial coulombic efficiency of full-cell is effectively enhanced from 69.2% to 91.7% and the first discharge capacity increases from 120.4 to 154.3 mAh·g$^{-1}$ (Figs. 4(c) and 4(d)). To furtherly explain the pre-

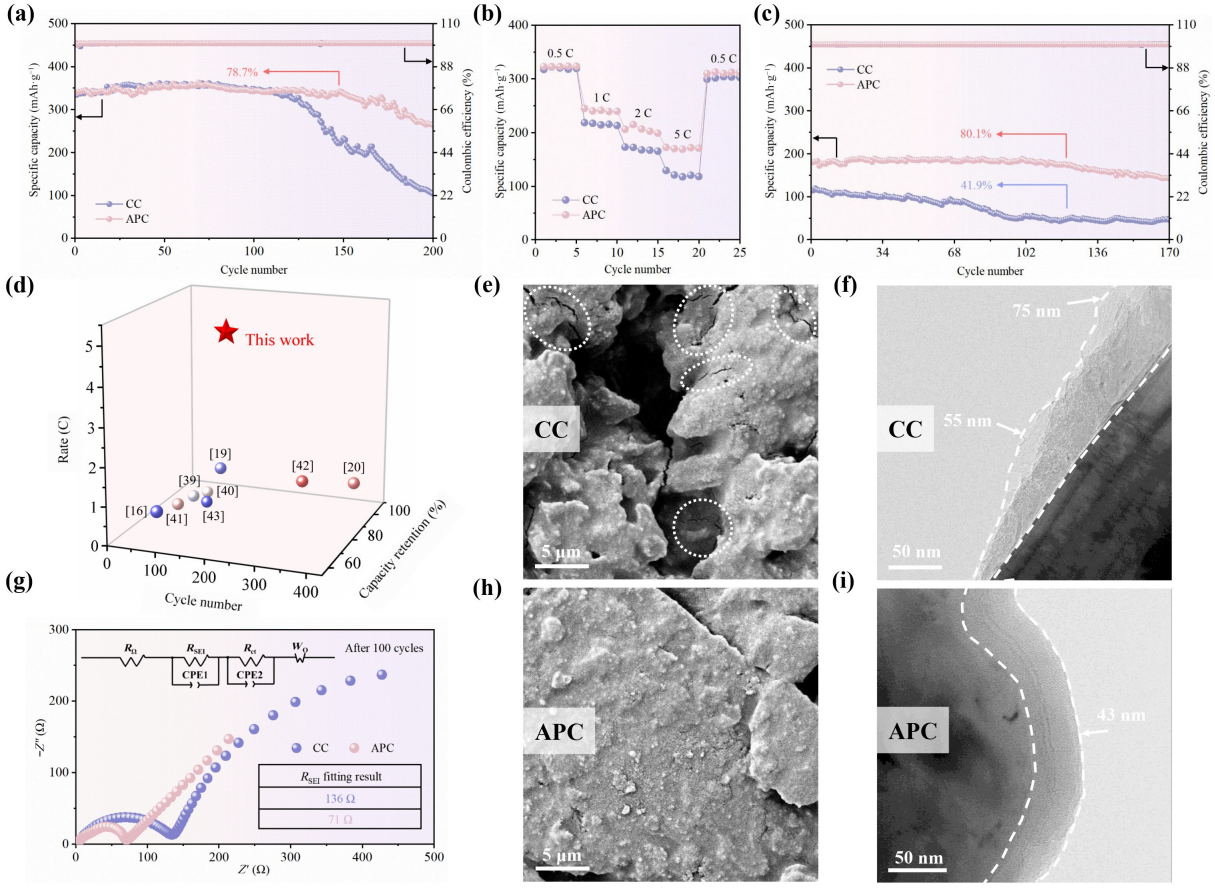


**Figure 3** Electrochemical performance of Li/Gr half cells under APC and CC discharge. (a) Cycling performance at 0.5 C. (b) Rate capability. (c) Cycling performance at 5 C. (d) Performance comparison with cells reported in typical literatures. (e) and (h) SEM and (f) and (i) TEM images of the electrodes after 100 cycles under (e) and (f) CC and (h) and (i) APC. (g) Comparison of EIS curves for Li/Gr formed under CC and APC after100 cycles.

lithiation process and effect of APC pre-formed $Li_2CO_3$-rich SEI, we compare the content variation of the main components in the different SEI using Li 1s (Fig. 4(e)) and O 1s (Fig. 4(f)) XPS. As the results comparison shown in Figs. 4(g) and 4(h), compared with the CC-formed Gr anode (CC), the APC-formed Gr (APC) and APC pre-formed Gr extracted from the half-cell (APC-Gr) show significantly enhanced signals corresponding to $Li_2CO_3$, 55.7 eV in the Li 1s and C=O bonds in the O 1s spectrum [37], confirming that the APC mode promotes the thorough conversion of $CO_2$ into $Li_2CO_3$, thereby constructing a $Li_2CO_3$-rich SEI. Moreover, relative to that formed in the half-cell, the $Li_2CO_3$ contents of APC-Gr anode in the full cell remains essentially unchanged. In the Li 1s spectrum, it is observed to be between 58% and 59%, in the O 1s spectrum, it ranges from 46% to 48%. These corroborate that the APC pre-formed $Li_2CO_3$-rich SEI undergoes no significant reconstruction or thickening during full-cell operation, thereby it will not continuously consume the limited active lithium in the full-cell. Consequently, owing to the APC pre-formed high-quality SEI on the Gr anode from the half-cell, the LFP/APC-Gr full cell retains a discharge capacity of 131.8 mAh·g$^{-1}$ with 90% capacity retention after 100 cycles at 0.5 C, increasing 39.5% in capacity and 10% in retention compared with the LFP/Gr full cell (Fig. 4(i)). These results highlight the superiority of the present strategy. Direct application of the APC charge to promote $CO_2$ reduction in a full cell would consume a substantial amount of the limited active lithium, leading to severe losses in initial efficiency and capacity. While this pre-lithiation strategy adopted here utilizes the abundant lithium source from the Li metal in a half-cell and APC protocol to pre-construct a stable, high-quality SEI on the Gr anode. This effectively decouples the lithium consumption required for SEI formation from the active lithium in the full-cell, therefore successfully enhancing the initial coulombic efficiency and improving the usable capacity and long-term cycling stability of the full cell.

## 4 Conclusion

This work first reveals that during the use of gaseous $CO_2$ as an additive for constructing the SEI on Gr anodes, the interfacial adsorption and accumulation of the intermediate product CO constitute a key kinetic bottleneck, which limits the complete reduction of $CO_2$ and impedes the formation of a high-performance $Li_2CO_3$-rich SEI. Therefore, we then develop a simple yet effective APC discharge strategy in the first discharge to drive $CO_2$ reduction, by which periodically switched electrical fields regulate the interfacial microenvironment and accelerate the desorption and diffusion of the CO intermediate, and significantly promote the conversion efficiency of $CO_2$ into $Li_2CO_3$, successfully resulting in the *in-situ* formation of a uniform, smooth, and $Li_2CO_3$-rich SEI layer on the Gr surface. Attributed to the excellent electrical-mechanical stability and higher $Li^+$ conductivity of $Li_2CO_3$-rich SEI formed by APC, Li/Gr half-cells deliver exceptional cycling stability and rate performance (80.1% capacity retention after 170 cycles at 5 C). Moreover, employing the Gr anode with APC pre-formed SEI to assemble LFP/Gr full cell can effectively compensate the active

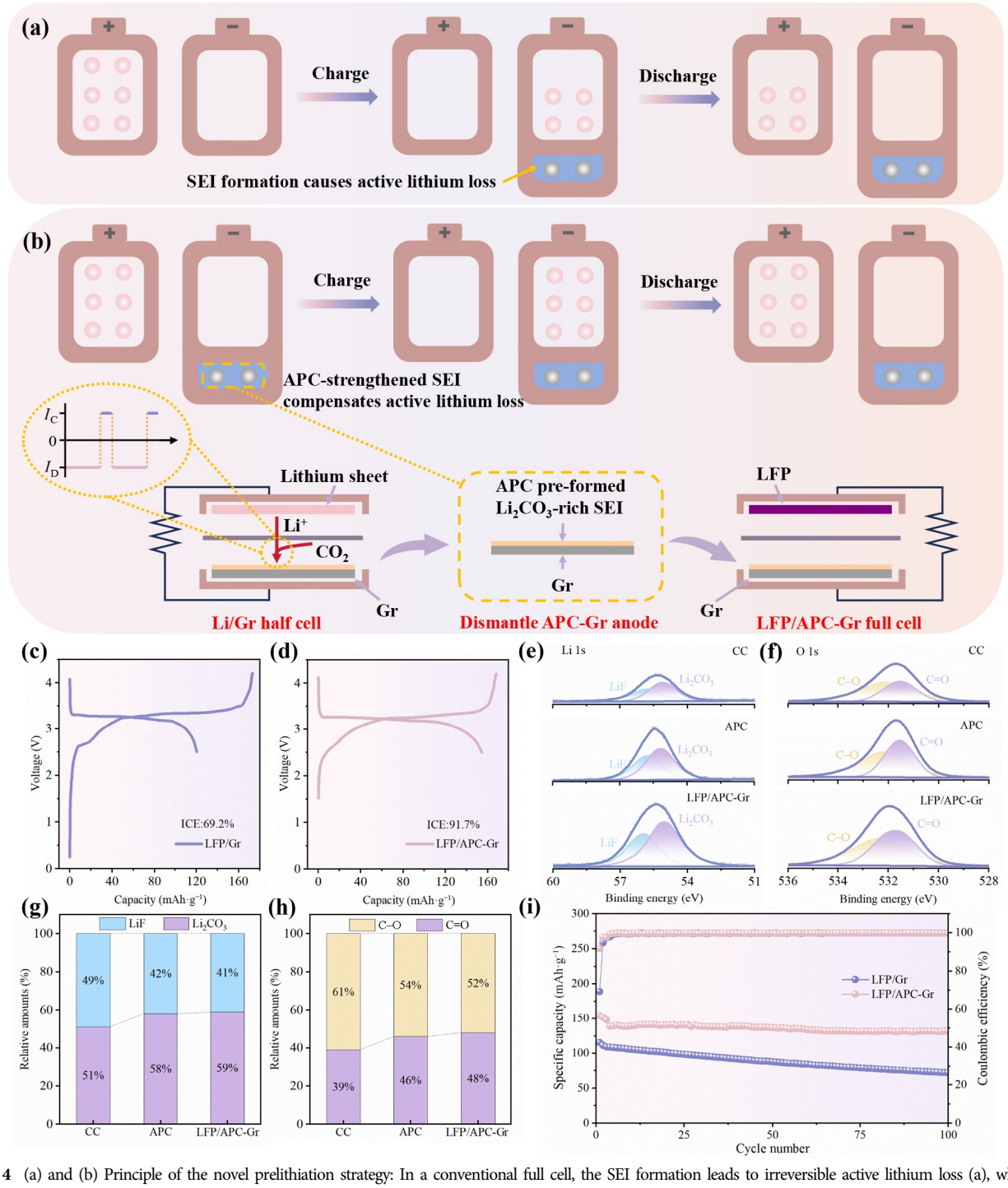


**Figure 4** (a) and (b) Principle of the novel prelithiation strategy: In a conventional full cell, the SEI formation leads to irreversible active lithium loss (a), while the developed prelithiation method addresses this issue by pre-constructing a $Li_2CO_3$-rich SEI on the Gr anode in a Li/Gr half-cell using the APC strategy, and then this APC pre-formed Gr anode is used to assemble LFP/Gr full cell, thereby avoiding the initial irreversible active lithium loss during the full-cell cycles. (c) and (d) The initial charge/discharge curves. XPS characterization of SEI components formed under three different conditions: after 5 cycles in APC mode, after 5 cycles in CC mode, and after 5 cycles in a full cell re-assembled with an APC-prefilmed electrode: (e) and (f) Li 1s and O 1s spectra. (g) and (h) Comparison of Li 1s and O 1s XPS peak areas. (i) The cycling performance of the lithium-ion full batteries with LFP as a cathode.

lithium loss caused by SEI formation, not only enhancing the initial coulombic efficiency from 69.2% to 91.7%, but also substantially increasing the discharge capacity and long-term cycling performance (remains 131.8 mAh·g$^{-1}$ with 90% capacity retention after 100 cycles) due to this high-quality SEI formed in advance. By developing a novel external field regulation strategy to improve the utilization efficiency of gaseous additives, this work opens a new avenue for high-performance LIBs from the techniques of interphase regulation and electrolyte formulation optimization.

**Electronic Supplementary Material**: Supplementary material (additional SEM images, TEM images, SECM, AFM, *in-situ* DEMS,

EIS, ICP-OES, and electrochemical performance data) is available in the online version of this article at https://doi.org/10.26599/NR.2026.94908818.

## Acknowledgements

This work was supported by the National Natural Science Foundation of China (No. 22269012), Key Research and Development Program of Gansu (No. 24YFGA025), and Baiyin Key Science and Technology plan (No. 2025-1-62G).

## Declaration of competing interest

All the contributing authors report no conflict of interests in this work.

## Author contribution statement

Y. Q. K.: Validation, writing – original draft. S. Y. L.: Supervision, writing – review & editing. P. W.: Conceptualization, supervision. Y. Q.: Investigation. H. H. Y.: Visualization. D. D. H.: Visualization. L. J. W.: Supervision. J. B.: Supervision. T. T. L.: Investigation. D. N. Z.: Resources, investigation. X. L. C.: Supervision, writing – review & editing. All authors approved the final version of the manuscript.

## Use of AI statement

None.

## References

[1] Armand, M.; Tarascon, J. M. Building better batteries. *Nature* **2008**, *451*, 652–657.

[2] Yabuuchi, N.; Kubota, K.; Dahbi, M.; Komaba, S. Research development on sodium-ion batteries. *Chem. Rev.* **2014**, *114*, 11636–11682.

[3] Rudola, A.; Sayers, R.; Wright, C. J.; Barker, J. Opportunities for moderate-range electric vehicles using sustainable sodium-ion batteries. *Nat. Energy* **2023**, *8*, 215–218.

[4] Wang, P.; Yang, H. H.; Ding, H.; Zhang, N. S.; Zhao, D. N.; Li, S. Y. Application of *in-situ* characterization techniques and artificial intelligence-assisted analysis in studying electrode/electrolyte interface of batteries. *Mater. Sci. Eng.: R: Rep.* **2026**, *168*, 101154.

[5] Cao, Y. L.; Li, M.; Lu, J.; Liu, J.; Amine, K. Bridging the academic and industrial metrics for next-generation practical batteries. *Nat. Nanotechnol.* **2019**, *14*, 200–207.

[6] Li, S. Y.; Li, J. N.; Wang, P.; Ding, H.; Zhou, J. F.; Li, C. Y.; Cui, X. L. Interface engineering regulation by improving self-decomposition of lithium salt-type additive using ultrasound. *Adv. Funct. Mater.* **2024**, *34*, 2307180.

[7] Xu, K. Li-ion battery electrolytes. *Nat. Energy* **2021**, *6*, 763–763.

[8] Zhao, D. N.; Liang, H. C.; Wu, S. M.; Quan, Y.; Hu, X. Y.; Li, J. N.; Wang, P.; Cui, X. L.; Li, S. Y. Customizing solid electrolyte interphase with bilayer spatial structure to mitigate swelling towards long-term life lithium battery. *J. Energy Chem.* **2025**, *105*, 702–712.

[9] Jagger, B.; Pasta, M. Solid electrolyte interphases in lithium metal batteries. *Joule* **2023**, *7*, 2228–2244.

[10] Wang, Z. X.; Sun, Z. H.; Shi, Y.; Qi, F. L.; Gao, X. N.; Yang, H. C.; Cheng, H. M.; Li, F. Ion-dipole chemistry drives rapid evolution of Li ions solvation sheath in low-temperature Li batteries. *Adv. Energy Mater.* **2021**, *11*, 2100935.

[11] Chen, Y. C.; Ouyang, C. Y.; Song, L. J.; Sun, Z. L. Electrical and lithium ion dynamics in three main components of solid electrolyte interphase from density functional theory study. *J. Phys. Chem. C* **2011**, *115*, 7044–7049.

[12] Brown, Z. L.; Jurng, S.; Nguyen, C. C.; Lucht, B. L. Effect of fluoroethylene carbonate electrolytes on the nanostructure of the solid electrolyte interphase and performance of lithium metal anodes. *ACS Appl. Energy Mater.* **2018**, *1*, 3057–3062.

[13] Jurng, S.; Brown, Z. L.; Kim, J.; Lucht, B. L. Effect of electrolyte on the nanostructure of the solid electrolyte interphase (SEI) and performance of lithium metal anodes. *Energy Environ. Sci.* **2018**, *11*, 2600–2608.

[14] Lan, X. X.; Cui, J.; Xiong, X. Y.; He, J. Y.; Yu, H. C.; Hu, R. Z. Multiscale observations of inhomogeneous bilayer SEI film on a conversion-alloying $SnO_2$ anode. *Small Methods* **2021**, *5*, 2101111.

[15] Choi, Y. K.; Chung, K. I.; Kim, W. S.; Sung, Y. E.; Park, S. M. Suppressive effect of $Li_2CO_3$ on initial irreversibility at carbon anode in Li-ion batteries. *J. Power Sources* **2002**, *104*, 132–139.

[16] Bhattacharya, S.; Riahi, A. R.; Alpas, A. T. Electrochemical cycling behaviour of lithium carbonate ($Li_2CO_3$) pre-treated graphite anodes - SEI formation and graphite damage mechanisms. *Carbon* **2014**, *77*, 99–112.

[17] Cavanagh, A. S.; Lee, Y.; Yoon, B.; George, S. Atomic layer deposition of LiOH and $Li_2CO_3$ using lithium t-butoxide as the lithium source. *ECS Trans.* **2010**, *33*, 223–229.

[18] Aurbach, D.; Ein-Eli, Y.; Chusid, O.; Carmeli, Y.; Babai, M.; Yamin, H. The correlation between the surface chemistry and the performance of Li - carbon intercalation anodes for rechargeable 'rocking - chair' type batteries. *J. Electrochem. Soc.* **1994**, *141*, 603–611.

[19] Bläubaum, L.; Röse, P.; Schmidt, L.; Krewer, U. The effects of gas saturation of electrolytes on the performance and durability of lithium-ion batteries. *ChemSusChem* **2021**, *14*, 2943–2951.

[20] Zhang, Y.; Wang, L. Z.; Feng, H.; Zhang, A. Q.; Zhang, C. F.; Zhang, P. Effect of $SO_2$ and $CO_2$ additives on the cycle performances of commercial lithium-ion batteries. *Ionics* **2011**, *17*, 677–682.

[21] Pan, Y. R.; Yu, H.; Zhang, Y.; Wang, Z. K.; Wang, S.; Li, C.; Ma, Y.; Shi, X. X.; Zhang, H. Z.; Song, D. W. et al. In-depth exploration of the effect mechanisms of various lithium salt anions in solid-state and liquid lithium metal batteries. *J. Mater. Chem. A* **2024**, *12*, 16447–16456.

[22] Li, S. Y.; Zhang, Y. L.; Wu, S. M.; Quan, Y.; Wu, M. L.; Wang, P.; Zhao, D. N.; Cui, X. L. Synchronized achieving amount reduction and efficiency increase of lithium salt-type additive by alternating current pulse discharge technology. *Chem. Eng. J.* **2024**, *485*, 150095.

[23] Zhang, Y. L.; Li, S. Y.; Wu, M. L.; Wang, L. J.; He, N.; Quan, Y.; Wang, P.; Zhao, D. N.; Cui, X. L. Construct favorable solid electrolyte interphase by applying alternating current discharge during battery formation. *Chem. Eng. J.* **2025**, *510*, 161738.

[24] Schwenke, K. U.; Solchenbach, S.; Demeaux, J.; Lucht, B. L.; Gasteiger, H. A. The impact of $CO_2$ evolved from VC and FEC during formation of graphite anodes in lithium-ion batteries. *J. Electrochem. Soc.* **2019**, *166*, A2035–A2047.

[25] Wu, S. M.; Zhang, Y. L.; Liang, H. C.; Pan, H. J.; Chen, L.; Jiang, Y. X.; Ding, H.; Wang, P.; Zhao, D. N.; Zhang, Q. et al. *In-situ* electrochemical customization of solid electrolyte interphase for fast-charging and long-cycle-life graphite anodes. *Energy Storage Mater.* **2025**, *75*, 104024.

[26] Zhao, D. N.; Song, L. H.; Wang, J.; Zhang, J. J.; Cui, X. L.; Wang, P.; Sun, J. L.; Cai, X. P.; Huang, J.; Zhang, N. S. et al. Insight into the competitive reaction between LiDFP and LiFSI in lithium-ion battery at low temperature. *J. Power Sources* **2022**, *549*, 232147.

[27] Wang, J.; Lu, H. L.; Zhang, J. J.; Li, S. Y. Improved interfacial property of $Na_3V_2(PO_4)_3$@C cathode: Application of NaODFB-based ether electrolyte in sodium-ion batteries. *J. Electrochem. Energy Convers. Storage* **2023**, *20*, 011005.

[28] Chen, J.; Quattrocchi, E.; Ciucci, F.; Chen, Y. H. Charging processes in lithium-oxygen batteries unraveled through the lens of the

distribution of relaxation times. *Chem* **2023**, *9*, 2267–2281.
[29] Cui, X. L.; Hu, X. Y.; Wang, P.; Zhao, D. N.; Wang, M. Y.; Li, J. N.; Liang, H. C.; Sun, M. Z.; Yao, Y. J.; Li, S. Y. Accurately predicting decomposition potential of electrolyte additives by voltage relaxation curve analysis. *Chem. Eng. J.* **2025**, *507*, 160884.
[30] Zhuang, G. R.; Chen, Y. F.; Ross, P. N. Jr. The reaction of lithium with carbon dioxide studied by photoelectron spectroscopy. *Surf. Sci.* **1998**, *418*, 139–149.
[31] Ahmadiparidari, A.; Warburton, R. E.; Majidi, L.; Asadi, M.; Chamaani, A.; Jokisaari, J. R.; Rastegar, S.; Hemmat, Z.; Sayahpour, B.; Assary, R. S. et al. A long-cycle-life lithium-$CO_2$ battery with carbon neutrality. *Adv. Mater.* **2019**, *31*, 1902518.
[32] Chen, B.; Wang, D. S.; Tan, J. Y.; Liu, Y. Q.; Jiao, M. L.; Liu, B. L.; Zhao, N. Q.; Zou, X. L.; Zhou, G. M.; Cheng, H. M. Designing electrophilic and nucleophilic dual centers in the $ReS_2$ plane toward efficient bifunctional catalysts for Li–$CO_2$ batteries. *J. Am. Chem. Soc.* **2022**, *144*, 3106–3116.
[33] Yao, Y. J.; Wang, P.; Zhao, Y. J.; Zhang, J. W.; Hu, L.; Zhou, J. F.; Wang, Y. N.; Dou, H. Z.; Luo, J.; Li, S. Y. et al. Efficient decomposition of electrolyte salt reconstructing Helmholtz plane for long life sodium-ion batteries. *ACS Sustainable Chem. Eng.* **2025**, *13*, 4439–4448.
[34] Li, S. Y.; Wang, L. J.; Zhang, Y. L.; Wang, H.; Kong, Y. Q.; Bai, J.; Lu, T. T.; Zhang, N. S.; Wang, P.; Cui, X. L. Alternative pulse current charging reinforcing the cathode-electrolyte interphase to inhibit the aluminum corrosion of LiFSI-based batteries at high temperatures. *ACS Sustainable Chem. Eng.* **2026**, *14*, 7878–7887.
[35] Zhu, T. H.; Hu, Q. Y.; Yan, G. C.; Wang, J. X.; Wang, Z. X.; Guo, H. J.; Li, X. H.; Peng, W. J. Manipulating the composition and structure of solid electrolyte interphase at graphite anode by adjusting the formation condition. *Energy Technol.* **2019**, *7*, 1900273.
[36] Tian, J. X.; Lang, S. Y.; Liu, G. X.; Liu, R. Z.; Wang, J.; Li, Y.; Wen, R. *In situ* monitoring of dual-salt synergy in the cathode and anode processes in lithium metal batteries. *eSci. Energy* **2025**, *1*, 100004.
[37] Qin, N.; Jin, L. M.; Lu, Y. Y.; Wu, Q.; Zheng, J. S.; Zhang, C. M.; Chen, Z. H.; Zheng, J. P. Over-potential tailored thin and dense lithium carbonate growth in solid electrolyte interphase for advanced lithium ion batteries. *Adv. Energy Mater.* **2022**, *12*, 2103402.
[38] Yang, K. R.; Zhao, D. N.; Wang, H.; Hu, L.; Li, B. Q.; Cui, X. L.; Li, S. Y. Promoting long-term stability and high-temperature tolerance of lithium-ion batteries by introducing anion receptor additives into electrolyte. *J. Energy Storage* **2025**, *117*, 116094.
[39] Dai, X. Y.; Zhou, A. J.; Xu, J.; Lu, Y. T.; Wang, L. P.; Fan, C.; Li, J. Z. Extending the high-voltage capacity of $LiCoO_2$ cathode by direct coating of the composite electrode with $Li_2CO_3$ via magnetron sputtering. *J. Phys. Chem. C* **2016**, *120*, 422–430.
[40] Krause, L. J.; Chevrier, V. L.; Jensen, L. D.; Brandt, T. The effect of carbon dioxide on the cycle life and electrolyte stability of Li-ion full cells containing silicon alloy. *J. Electrochem. Soc.* **2017**, *164*, A2527–A2533.
[41] Shin, J. S.; Han, C. H.; Jung, U. H.; Lee, S. I.; Kim, H. J.; Kim, K. Effect of $Li_2CO_3$ additive on gas generation in lithium-ion batteries. *J. Power Sources* **2002**, *109*, 47–52.
[42] Bao, C. G.; Liu, Q.; Chen, H.; Zeng, Q.; Peng, K.; Wu, W.; Liu, H. B.; Li, B. H. Catalytic decomposition of ethylene carbonate by pyrrolic-N to stabilize solid electrolyte interphase on graphite anode under extreme conditions. *Nano Energy* **2024**, *127*, 109775.
[43] Li, C. K.; Xiao, Y.; Zhang, X. S.; Cheng, H. W.; Cheng, Y. J.; Xia, Y. G. $Li_2CO_3$ nanocomposites as cathode lithium replenishment material for high-energy-density Li-ion batteries. *ACS Appl. Mater. Interfaces* **2023**, *15*, 44921–44931.
[44] Zhan, R. M.; Wang, X. C.; Chen, Z. H.; Seh, Z. W.; Wang, L.; Sun, Y. M. Promises and challenges of the practical implementation of prelithiation in lithium-ion batteries. *Adv. Energy Mater.* **2021**, *11*, 2101565.
[45] Li, S.; Jiang, J. M.; Feng, Q. L.; Zheng, Y.; Chen, Y. X.; Ju, Z. C.; Zhuang, Q. C.; Wu, K.; Shao, H. Y.; Zhang, X. G. Molecular engineering chemical pre-lithiation reagent with low redox potential for graphite anode enables high Coulombic efficiency. *Small* **2024**, *20*, 2406274.
[46] Shen, Y. F.; Qian, J. F.; Yang, H. X.; Zhong, F. P.; Ai, X. P. Chemically prelithiated hard-carbon anode for high power and high capacity Li-ion batteries. *Small* **2020**, *16*, 1907602.
[47] Tan, R.; Liu, K. X.; Zhu, X. L.; Yang, S. Y.; Zhang, Q.; Zhang, J. Z.; Chang, Z.; Chai, P. C.; Wang, X. Z.; Fontaine, O. et al. Rational molecular design of aryl-lithium reagent enables precise chemical prelithiation of graphite anodes for achieving ideal 100% initial Coulombic efficiency. *J. Am. Chem. Soc.* **2025**, *147*, 21865–21876.